Retrieval of aerosol optical properties from OMI radiances using a multiwavelength algorithm: Application to western Europe

R. L. Curier,[1,2] J. P. Veefkind,[3] R. Braak,[3] B. Veihelmann,[3] O. Torres,[4] and G. de Leeuw[1,5,6]

[1]   The Ozone Monitoring Instrument (OMI) multiwavelength algorithm has been developed to retrieve aerosol optical depth using OMI-measured reflectance at the top of the atmosphere. This algorithm was further developed by using surface reflectance data from a field campaign in Cabauw (The Netherlands), a new cloud-screening method, and a global aerosol database derived from the aerosol transport model TM5. The first results from an application of this algorithm over western Europe are presented. The OMI-retrieved aerosol optical depth is evaluated by comparison with both ground-based measurements from Aerosol Robotic Network (AERONET) and Moderate Resolution Imaging Spectroradiometer (MODIS) satellite data. The various aerosol optical depth values compare favorably, except in situations where large changes occur in the surface properties, which is illustrated over the Iberian peninsula. OMI and MODIS aerosol optical depth are well correlated (with a correlation coefficient of 0.66 over land and 0.79 over sea), although the multiwavelength algorithm appears to overestimate the aerosol optical depth values with respect to MODIS. The multiwavelength algorithm performs better over sea than over land. Qualitatively, the multiwavelength algorithm well reproduces the expected spatial aerosol optical depth gradient over western Europe.

1.   Introduction

[2]   The influence of aerosols on the Earth's radiative balance is one of the largest unknowns in the climate system. Aerosols have a direct effect by scattering and/or absorbing the incoming solar radiation [*Haywood and Boucher*, 2000]. The aerosols' net effect on the Earth's radiative balance depends on the aerosol chemical and physical properties, the surface albedo and the aerosol layer's altitude [*Torres et al.*, 1998]. The uncertainty in the effect of aerosols on climate stems from the large variability of aerosol sources, i.e., their concentrations and physical, chemical and optical properties, in combination with their short atmospheric residence time of a few days. Experimental data on aerosol properties are available from ground-based observations. However, they often are only representative for local situations and cannot be used for estimates of effects on regional to global scales. Furthermore, they are part of several networks which often are disconnected and the data are available in different formats, on different time scales and measured using different procedures and correction factors. Although efforts have been made to harmonize some of these data sets (e.g., Global Atmosphere Watch (GAW) program of the World Meteorological Organization (WMO), www.wmo.ch/web/arep/gaw/gaw_home.html) and EMEP (cooperative program for monitoring and evaluation of the long-range transmission of air pollutants in Europe through the European project CREATE, http://www.gse-promote.org/services/create/createdb.html), the data availability on a global or regional scale is still a concern. Furthermore, the area coverage is very sparse for most continents. An alternative to provide aerosol properties on a regional to global scale with a spatial resolution varying from 1×1 km^2 to $1° \times 1°$ and a temporal resolution of once per day is provided by Sun synchronous satellites. Satellite data insure the creation of worldwide aerosol database properties derived from the same protocol. The use of satellites is complementary to the ground-based networks for extension to larger spatial scales, even though the satellite-retrieved aerosol properties do not provide the same detail and accuracy as ground-based in situ measurements and lack vertical resolution (except for spaceborne lidars such

[1]TNO Defence, Safety and Security, The Hague, Netherlands.
[2]Now at Atmospheric Modeling and Observations, Climate Change Unit, Finnish Meteorological Institute, Helsinki, Finland.
[3]KNMI, De Bilt, Netherlands.
[4]NASA Goddard Space Flight Center, Greenbelt, Maryland, USA.
[5]Research and Development, Finnish Meteorological Institute, Helsinki, Finland.
[6]Department of Physical Sciences, University of Helsinki, Helsinki, Finland.

as the Cloud-Aerosol Lidar with Orthogonal Polarization (CALIOP)).

[3] The Ozone Monitoring Instrument (OMI) is a Dutch-Finnish contribution to the Aura mission [*Schoeberl et al.*, 2006]. It is a nadir-viewing spectrometer that measures solar reflected and backscattered light in the UV-visible domain between 270 nm and 500 nm [*Levelt et al.*, 2006a, 2006b]. The reflectance at the top of the atmosphere (TOA) measured by OMI is used to derive aerosol optical properties, two algorithm has been developed to achieve this goal. The Near-UV algorithm (OMI-Aerosol Ultraviolet, OMAERUV [*Torres et al.*, 2002a]), which uses two wavelengths in the near-UV to provide the aerosol optical depth and the single scattering albedo at 388 nm. The Near-UV method was initially developed to retrieve aerosol properties from Total Ozone Mapping Spectrometer (TOMS) observations and has been upgraded for OMI as explained by *Torres et al.* [2002b]. The Near-UV method is based on the difference in the sensitivity of the TOA radiation at two wavelength bands to absorbing aerosols such as carbonaceous aerosols or mineral dust and can be applied over any surface. The multiwavelength method (OMI-AEROsol, OMAERO) is a new approach, which exploits the information in the wider wavelength range between 330 nm and 500 nm. In the current implementation of the multiwavelength algorithm, 14 wavelength bands between 342.5 nm and 483.5 nm are used. This choice has been made in order to exclude spectral features in the surface albedo related to surface vegetation and ozone absorption features in the UV. The aerosol optical depth is retrieved for a number of aerosols models and a best fitting aerosol model is determined. It has been theoretically shown that OMI spectral reflectance measurements in the mentioned wavelength bands content between 2 and 4 degrees of freedom and are sensitive to aerosol parameters such as the aerosol optical depth and the single-scattering albedo [*Veihelmann et al.*, 2007].

[4] The main goal of this study is to validate the aerosol optical depth output of the multiwavelength algorithm, therefore,in agreement with the study made by *Veihelmann et al.* [2007], which pointed out the redundancy of the information contain in the nominal wavelengths, the retrievals in this study were made over Western Europe for May to July 2005 for eight wavelengths of 342.5, 367.0, 388.0, 406.0, 425.5, 442.0, 463.0, and 471.0 nm. The aerosol optical depth provides information on the total concentration of particles for a given size range and its spectral variation provides an indication of the particle size distribution.

[5] In the near ultraviolet and visible domains the net aerosol effect on the TOA radiation results from complex interactions between several competing radiative processes: the scattering and absorption of incoming solar radiation by molecules and aerosols, the absorption of the scattered radiation, scattering and absorption of radiation reflected by the underlying surface. For OMI wavelengths in the near UV and the visible almost all surfaces (except ice, snow, desert and salt lakes), have low surface albedo. Therefore, for cloud-free skies, the TOA radiance is dominated by atmospheric effects, i.e., molecular and aerosol scattering and absorption.

[6] In this paper, we present the first results from the retrieval of aerosol optical depth from application of the multiwavelength algorithm [*Torres et al.*, 2002b] to Ozone Monitoring Instrument (OMI) data over western Europe for

May to July 2005. An extended version of the multiwavelength algorithm is presented and validated. Section 2 gives an overview of the different aerosol properties present in the OMAERO product derived from the multiwavelength algorithm. The extended version of the multiwavelength algorithm required an improvement of the cloud screening, an evaluation of the surface albedo effects on the TOA reflectance and the introduction of an improved aerosol climatology. The surface albedo was evaluated on the basis of experimental data. The cloud screening has been enhanced by the synergistic use of Moderate Resolution Imaging Spectroradiometer (MODIS) and OMI cloud masks. And finally, the aerosol geographical distribution has been improved using an aerosol transport model. The multiwavelength method as well as the different adjustments are explained in section 3. Results are presented in section 4. The aerosol optical depth time series for ten European sites are presented and evaluated versus Aerosol Robotic Network (AERONET) data [*Holben et al.*, 1998] in section 4.1. In sections 4.2 and 4.3, the OMI-retrieved aerosol optical depth is compared to MODIS-retrieved aerosol optical depth and the spatial variation of the aerosol optical depth over Europe is evaluated on the basis of monthly composite maps.

2. OMI Aerosol Product OMAERO

[7] OMI measurement are unique, they are sensitive to aerosol absorption in the UV and, at the same time, combine a small footprint (13 km × 24 km at nadir) with global coverage. The small footprint is essential for the observation of tropospheric aerosols. The UV absorption facilitates the distinction of aerosols types such as desert dust and biomass burning from other aerosol types.

[8] The OMI multiwavelength algorithm, OMAERO, provides aerosol optical depth, τ, and the most probable aerosol model for a given spectral reflectance measurement. The product comprises also the single-scattering albedo ω_0, layer height and the size distribution associated with the best fitting aerosol model. In addition, the aerosol indices in the UV and in the visible range for the main aerosol type are given for both clear and cloudy pixels.

[9] The extinction coefficient, σ_{ex}, describes the extinction of the incoming radiation at wavelength, λ, per unit length due to scattering and absorption by particles. σ_{ex} is expressed in km^{-1}

$$\sigma_{ex}(\lambda, m) = \int_0^\infty \pi r^2 Q_{ex}(\lambda, m, r) n(r) dr \qquad (1)$$

Q_{ex} is the extinction efficiency, for a single particle characterized by its radius r and complex refractive index m, at wavelength λ. $n(r)$ describes the number size distribution, i.e., the number concentration of particles for each radius r.

[10] The aerosol optical depth is defined as the column integrated aerosol extinction coefficient, i.e., integrated over the whole atmospheric column with height h, and is dimensionless.

$$\tau(\lambda, m) = \int_0^h \sigma_{ex}(\lambda, m, z) dz \qquad (2)$$

[11] The ratio of scattering to extinction is called the single scattering albedo, $\omega_0(\lambda, m)$, and is a measure for the
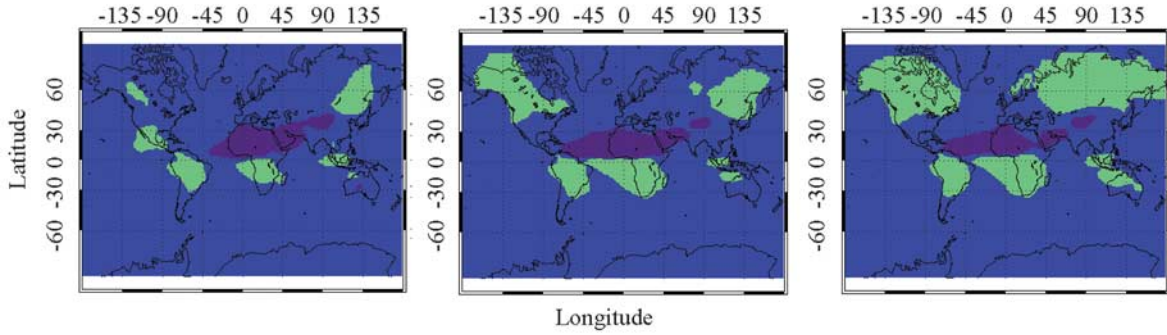
Figure 1. Aerosol geographical distribution for (left) May, (middle) June, and (right) July, determined using the chemical transport model (TM5) as described in the text, providing the climatology used as input in the OMI multiwavelength algorithm. Blue represents weakly absorbing aerosol, green indicates the occurrence of carbonaceous aerosol, and purple shows the occurrence of mineral aerosol.

amount of absorption relative to the total extinction. The value of the single scattering albedo is 1 when the extinction is solely due to scattering and 0 if the extinction is due to absorption only.

$$\omega_0(\lambda, m) = \frac{\sigma_{sc}(\lambda, m)}{\sigma_{ex}(\lambda, m)} \qquad (3)$$

σ_{sc} is the scattering coefficient.

[12] The aerosol index, ai, is a concept based on TOMS observations in the near UV [*Torres et al.*, 1998]. The aerosol index, as defined in equation (4) below, is the residue between the measured radiance and the calculated one using the Lambert Equivalent Reflectivity (LER) assumption. Assuming a Rayleigh scattering atmosphere above a Lambertian surface, the Lambert Equivalent Reflectivity [*Herman and Celarier*, 1997] is defined as the value of the Lambertian spectral surface albedo for which the modeled and measured TOA reflectance are equal. The LER in the multiwavelength algorithm was determined using the radiative transfer code Doubling-Adding KNMI (DAK) [*de Haan et al.*, 1987; *Stammes*, 2000].

$$ai = -100 \log\left\{\left[\frac{I_{\lambda_1}}{I_{\lambda_2}}\right]_{meas}\right\} + 100 \log\left\{\left[\frac{I_{\lambda_1}\left(A_{LER_{\lambda_1}}\right)}{I_{\lambda_2}\left(A_{LER_{\lambda_2}}\right)}\right]_{calc}\right\} \qquad (4)$$

A_{LER} is the wavelength-dependent surface Lambert Equivalent albedo. The UV aerosol index at 388 nm is calculated using the following wavelengths $\lambda_1 = 342.5$ nm and $\lambda_2 = 388$ nm. The Visible aerosol index at 483.5 nm is calculated using the following wavelengths $\lambda_1 = 388$ nm and $\lambda_2 = 483.5$ nm. The aerosol indices represent the change in the spectral contrast with respect to a molecular atmosphere due to the presence of cloud and/or aerosol particles [*Torres et al.*, 2002b]. The aerosol index is sensitive to elevated absorbing aerosol layers such as Saharan dust and biomass burning aerosols [*de Graaf et al.*, 2005].

3. Multiwavelength Algorithm

[13] In the wavelength range observed by OMI and for cloud-free skies, the TOA radiance is dominated by atmo-

spheric effects, i.e., molecular and aerosol scattering and absorption. Molecular scattering is referred to as Rayleigh scattering which varies with the wavelength λ as λ^{-4}. For the OMI wavelengths Rayleigh scattering contributes significantly to the total TOA radiance. To account for this effect the radiative transfer model DAK [*de Haan et al.*, 1987; *Stammes*, 2000] that includes aerosols and multiple scattering, is applied.

[14] The multiwavelength algorithm comprises two models: an inversion model (section 3.1) where the actual retrieval is done and a forward model (section 3.2) where all a priori data needed to retrieve the optical properties are defined and/or computed using DAK. A variety of aerosol models, characterized by their chemical and physical properties, are introduced into DAK. The aerosol particles are assumed to be spherical so the aerosol extinction is calculated using Mie theory [*Mie*, 1908]. The retrieval of aerosol information from satellite data is done in various steps. The first step is to determine whether a pixel is cloud free. Next the contribution of the surface to the TOA reflectance needs to be determined. Then the atmospheric contributions to the TOA reflectance need to be separated for gases and aerosols. The aerosol optical depth is retrieved using an optimal estimation retrieval scheme for a number of aerosol models. Then the best fitting aerosol model is selected and used to determine the aerosol optical depth. For a more detailed explanation of the basic components of the algorithm the reader is referred to the OMI ATBD [*Torres et al.*, 2002b]. The extensions to better account for surface effects, different types of aerosols and clouds are explained below in sections 3.2 and 3.3.

3.1. Inversion Model

[15] The core of the OMI aerosol algorithm is the derivation of aerosol optical properties for cloud free pixels, which is accomplished by comparing the measured TOA reflectance to results from a radiative transfer model stored in look-up tables (LUT). This is done for selected aerosol models for which the difference between the measured and computed TOA reflectances at a number of wavelengths is minimized using least squares minimization. The model with the smallest residue is selected as representative for the pixel. Subsequently this information is used to determine the aerosol optical depth of that ground pixel. The

Table 1. Size Distributions and Refractive Indices of OMI Aerosol Models[a]

Model	$r_{g,1}$	$r_{g,2}$	$\sigma_{g,1}$	$\sigma_{g,2}$	x_2	Real	Imag
WA_{1101}	0.078	0.497	1.499	2.160	4.36e-4	1.4	5.0e-8
WA_{1102}	0.088	0.509	1.499	2.160	4.04e-4	1.4	5.0e-8
WA_{1103}	0.137	0.567	1.499	2.160	8.10e-4	1.4	5.0e-8
WA_{1104}	0.030	0.240	2.030	2.030	1.53e-2	1.4	5.0e-8
WA_{1201}	0.078	0.497	1.499	2.160	4.36e-4	1.4	0.004
WA_{1202}	0.088	0.509	1.499	2.160	4.04e-4	1.4	0.004
WA_{1203}	0.137	0.567	1.499	2.160	8.10e-4	1.4	0.004
WA_{1301}	0.078	0.497	1.499	2.160	4.36e-4	1.4	0.012
WA_{1302}	0.088	0.509	1.499	2.160	4.04e-4	1.4	0.012
WA_{1303}	0.137	0.567	1.499	2.160	8.10e-4	1.4	0.012
BB_{2101}	0.074	0.511	1.537	2.203	1.70e-4	1.5	0.010
BB_{2102}	0.087	0.567	1.537	2.203	2.06e-4	1.5	0.010
BB_{2103}	0.124	0.719	1.537	2.203	2.94e-4	1.5	0.010
BB_{2201}	0.074	0.511	1.537	2.203	1.70e-4	1.5	0.020
BB_{2202}	0.087	0.567	1.537	2.203	2.06e-4	1.5	0.020
BB_{2203}	0.124	0.719	1.537	2.203	2.94e-4	1.5	0.020
BB_{2301}	0.074	0.511	1.537	2.203	1.70e-4	1.5	0.030
BB_{2302}	0.087	0.567	1.537	2.203	2.06e-4	1.5	0.030
BB_{2303}	0.124	0.719	1.537	2.203	2.94e-4	1.5	0.030
DD_{3101}	0.042	0.670	1.697	1.806	4.35e-3	1.53	$\lambda\text{-}dep.$*
DD_{3102}	0.052	0.670	1.697	1.806	4.35e-3	1.53	$\lambda\text{-}dep.$*
DD_{3201}	0.042	0.670	1.697	1.806	4.35e-3	1.53	$\lambda\text{-}dep.$#
DD_{3202}	0.052	0.670	1.697	1.806	4.35e-3	1.53	$\lambda\text{-}dep.$#
VO_{4101}	0.230	0.230	0.800	0.800	0.5	1.45	7.5e-7

[a]The aerosol types (weakly absorbing, WA; carbonaceous, BB; minerals, DD) provide different aerosol models according to size distribution, refractive index, and vertical distribution. An extra aerosol type is added to account for volcanic ashes (VO). Geometric mean radii, r_g, and geometric standard deviation, σ_g, of modes 1 and 2 of the bimodal size distribution are listed together with the particle number fraction x_2 of the second mode. The imaginary part of the refractive index of desert dust is wavelength dependent and takes values up to 6.53e-3 (*) or 0.013 (#) in the UV.

selection of the aerosol models used in this procedure is based on maps providing the monthly averaged geographical distribution of the occurrence of certain aerosol types (see section 3.2.1).

3.2. Forward Model

[16] In the absence of clouds, the TOA reflectance measured by satellite sensors arises from atmospheric scattering (molecules and aerosol particles) and surface reflectance. The determination of aerosol optical properties from the measured TOA reflectance is an ill posed problem because there is insufficient information to constrain for possible solutions. Therefore, radiative transfer calculations using DAK are performed to derive the Rayleigh and surface contribution, and a priori assumptions are made on the aerosol. Radiative transfer calculations are time consuming, it is therefore convenient and common practice to use precalculated sets of radiative parameters in the algorithm [e.g., *Veefkind et al.*, 1998; *von Hoyningen-Huene et al.*, 2003; *Levy et al.*, 2007].

3.2.1. Geographical Aerosol Distribution

[17] To account for the aerosol spatial and temporal variability, a climatology has been prepared in which the aerosols are classified into different types according to their optical properties. Three generic classes are distinguished: weakly absorbing, carbonaceous and mineral aerosols. Sea salt, sulfate and nitrate are three major components of the weakly absorbing class. Sea salt is entirely natural whereas nitrate and sulfate can be of both natural and anthropogenic origin. Carbonaceous aerosols are generated by biomass burning and fossil fuel combustion. Their chemical composition is a mixture of both absorbing and nonabsorbing compounds. The UV-absorbing feature of carbonaceous

aerosols is mainly driven by the fraction of black carbon. Mineral aerosols are mechanically generated over the deserts. The presence of iron oxides in mineral dust is responsible for the absorption of UV radiation. The aerosol temporal and geographical distribution database used in the
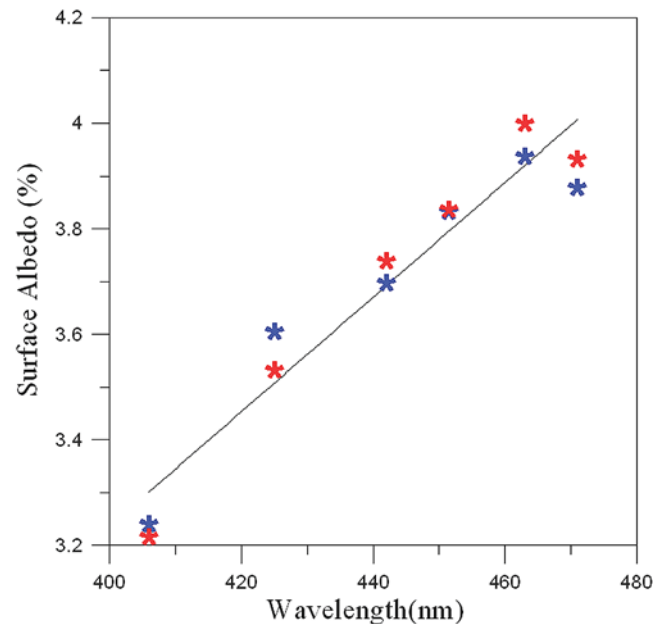

Figure 2. Surface albedo at the Cabauw site derived from the OMI signal for 19 June (blue) and 23 June (red) as described in the text.
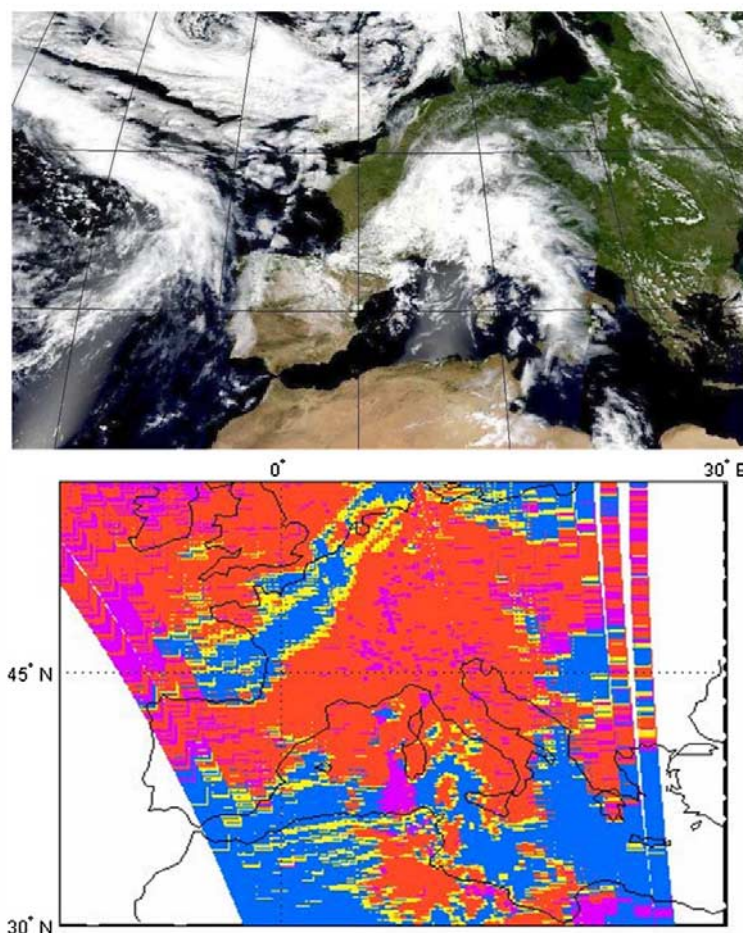
Figure 3. The top panel is a RGB picture derived from channels 1, 3, and 4 of MODIS for 14 June 2005. The bottom panel represents the OMI cloud mask, i.e., a composite map of the cloud mask derived by the multiwavelength algorithm for 14 June 2005. Pixels determined cloudy by all tests are red. Pixels determined cloudy by the cloud fraction threshold only are purple. Pixels which did not pass the homogeneity test are yellow. Clear pixels are blue.

multiwavelength algorithm has been developed with a 3-D chemical transport zoom model(TM5). The prescribed data set for the emissions of the primary aerosols in TM5 is presented by *Dentener et al.* [2006] and the model results used in this study were retrieved within the framework of the Aerosol Comparison between Observation and Models (AeroCom) project [*Kinne et al.*, 2006].

[18] This database has been developed on a grid of $1° \times 1°$. The weakly absorbing aerosols are assumed to be always present; the two other classes are indicated to be present when the ratio of their mass to the total mass is higher than a threshold, here set at 0.4. Figure 1 shows the resulting geographical distribution of the three aerosol types, used in the OMI multiwavelength algorithm, for the months of May, June and July. Carbonaceous aerosols mainly occur around heavily industrialized areas and over the tropical rain forests, where they are mainly known as biomass burning. Mineral aerosols are mainly located over the northern hemisphere, the Sahara desert, the Middle East and the

Gobi desert, and are often referred to as desert dust. Saharan dust is also transported to the Tropical North Atlantic Ocean and the Mediterranean Sea.

3.2.2. Aerosol Model

[19] In the part of the solar spectrum observed by OMI, the effects of aerosols on radiative transfer are determined by the size distribution and the complex refractive index of the aerosols (i.e., the chemical composition) and the altitude of the aerosol layers. The aerosol size distributions and chemistry used to build the aerosol model are derived from AERONET ground-based Sun photometer measurements [*Dubovik et al.*, 2002]. AERONET data are used because they are available for a wide range of conditions all over the globe, and were all derived from the same type of instrument: they apply to column integrated properties which are also measured by spaceborne instruments. In order to build the aerosol models, radiative transfer calculations were performed for some tie points. A tie point represents a node in the database. These tie points are defined by the scene
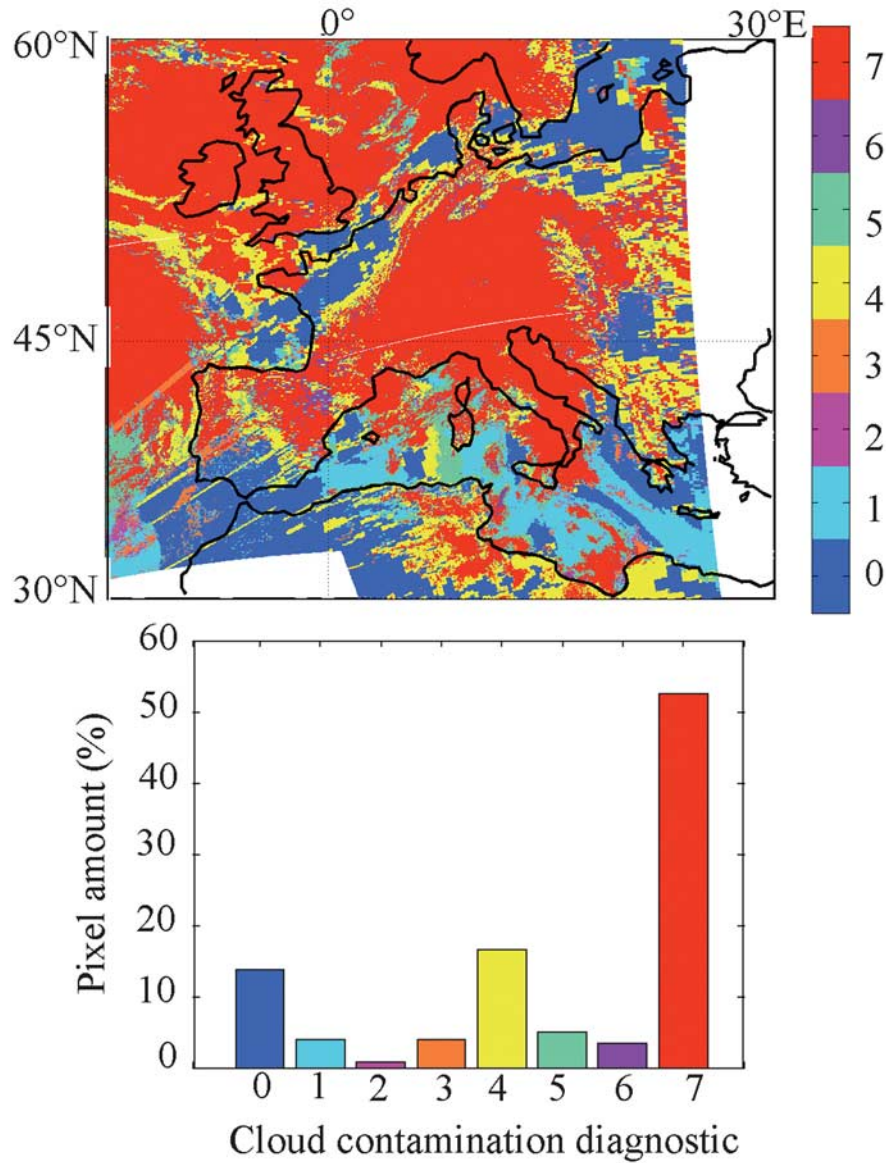
Figure 4. Comparison of the OMI and MODIS cloud screening for 14 June 2005. Dark blue and red represent pixels when MODIS and OMI diagnostics agree. Orange and yellow are representatives for pixels when OMI and MODIS disagree. The top panel is a composite map of the combined cloud mask. The bottom panel is a histogram of the number of pixels versus the cloud mask flag.

geometry, the surface and the aerosol optical properties. The aerosol size distribution is assumed to be the sum of two lognormal distributions following equation (5).

$$n(ln\ r) = \sum_{i=1}^{2} \frac{N_i}{(2\pi)^{\frac{1}{2}} ln\ \sigma_i} \exp\left(-\frac{(ln\ r_i - ln\ \bar{r}_{gi})^2}{2\ ln^2\ \sigma_i}\right) \quad (5)$$

where N_i is the number concentration, $\bar{r}_{gi}$ is the mean geometric radius and σ_i is the standard deviation of the *ith* lognormal mode. The different aerosol models were built according to three generic aerosol types defined earlier in section 3.2.1, weakly absorbing, carbonaceous and mineral. Within an aerosol type the aerosol models differ by either their chemical composition (i.e., refractive index) or their size distribution. Detailed information on the aerosol models, such as geometric mean radii r_g, geometric standard

Table 2. Flag Description of the Combined Cloud Mask[a]

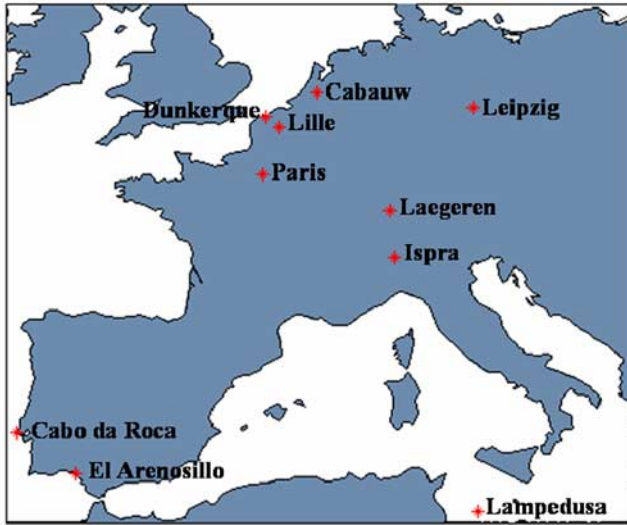| MODIS	OMI	COMBINED	Interpretation
0	0	0	clear for OMI and MODIS
1	0	1	probably clear for MODIS, clear for OMI
2	0	2	probably cloudy for MODIS, clear for OMI
3	0	3	cloudy for MODIS, clear for OMI
0	1	4	clear for MODIS, cloudy for OMI
1	1	5	probably clear for MODIS, cloudy for OMI
2	1	6	probably cloudy for MODIS, cloudy for OMI
3	1	7	cloudy for OMI and MODIS

[a]See Figure 4 (top).

Figure 5. Map of location of the AERONET site used in this study.

deviation σ_g, complex refractive index and the mode's fraction are presented in Table 1.

3.2.3. Surface Albedo

[20] The retrieval of aerosol optical depth requires precise information on the surface albedo. Uncertainties in the surface albedo lead to errors on the aerosol optical depth retrieval. *Veefkind et al.* [2000] estimated that in the UV range, an error of 0.01 in the surface albedo would induce an error of 0.1 in the aerosol optical depth retrieved. *Torres et al.* [1998] explained the impact of the surface albedo on the aerosol optical depth which is different for low and high

values. For high surface reflectivities the importance of aerosol absorption increases whereas the effect of scattering decreases significantly with the increase of the aerosol optical thickness. This is due to the enhancement of the ground reflection component that is backscattered by the aerosol layer toward the surface. For low surface albedo the impact depends on the absorption properties of the aerosol layer. If the aerosol layer is weakly absorbing, scattering dominates resulting in a net increase in the amount of backscattered radiation. If the aerosol layer is highly absorbing, a net decrease of the amount of backscattered radiation is observed. For more information the reader is referred to the OMI ATBD [*Torres et al.*, 2002b].

[21] The multiwavelength algorithm discriminates between land and sea pixels. The surface contribution to the reflectance at the top of the atmosphere is determined either by an ocean color model or by a surface albedo database for pixels over land.

[22] Currently available surface albedo databases are derived using TOMS [*Herman and Celarier*, 1997], Global Ozone Monitoring Experiment (GOME) [*Koelemeijer et al.*, 2003], Multiangle Imaging Spectroradiometer (MISR) [*Wanner et al.*, 1997] and MODIS data. GOME and TOMS surface albedo databases were derived using measured TOA albedo to derive the Minimum Lambert Equivalent Reflectivity (MLER) of the Earth's surface in the near UV and visible range. An atmospheric correction is applied to account for aerosols and molecules. However, owing to the large pixels size, the surface albedo databases from GOME and TOMS are affected by some cloud and aerosols contamination. MODIS [*Vermote and Vermeulen*, 1999] surface albedo is available at 470 nm and allows for aerosol
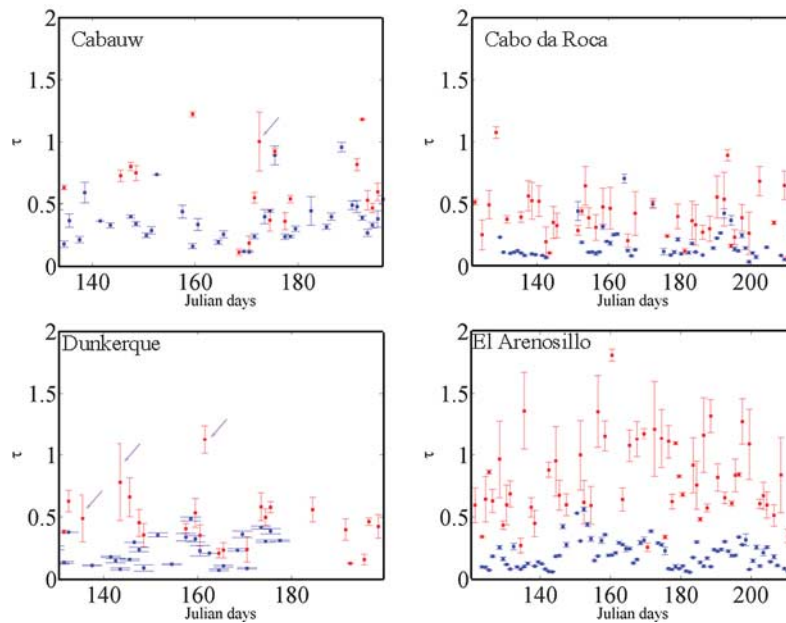

Figure 6. Time series of the aerosol optical depth for May to July 2005 for several AERONET sites in western Europe. The red squares represent the spatially averaged aerosol optical depth retrieved at 442 nm from the multiwavelength algorithm within a 50 km radius of the ground site, and the error bars denote its standard deviation. The blue squares represent the averaged aerosol optical depth measured between 1100 UTC and 1400 UTC at 440 nm with a Sun photometer.
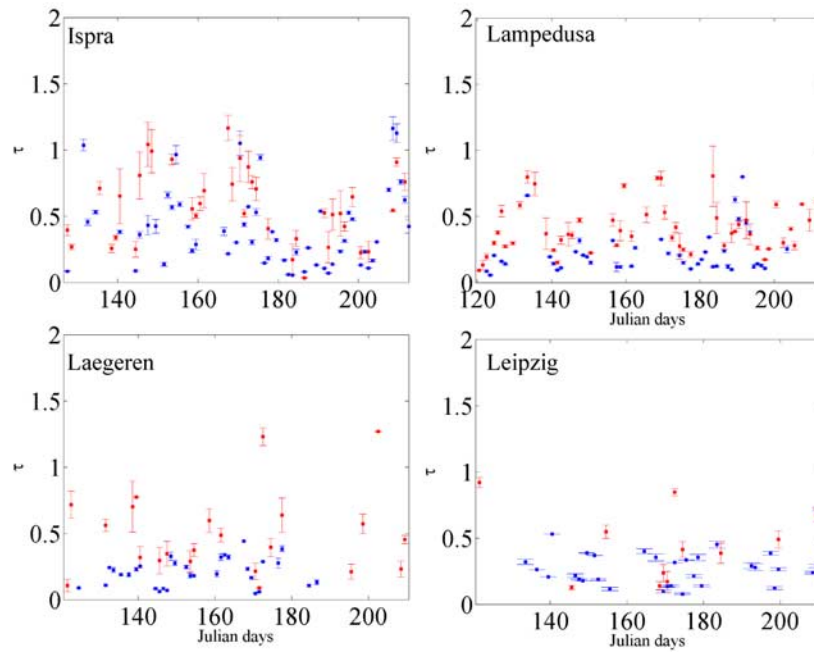
Figure 7. Time series at 442 nm continued.

correction and owing to a very high spatial resolution (500 m) cloud contamination is unlikely to happen.

[23] In order to determine which surface albedo database is suitable for use with OMI, the spectral dependence of surface albedo has been determined using data from the Dutch Aerosol and Nitrogen Dioxide Experiments for Validation of OMI and SCIAMACHY (DANDELIONS) [*Brinksma et al.*, 2005] campaign in Cabauw, The Netherlands. The TOA reflectances measured by OMI over Cabauw have been simulated for different surface reflectivities by means of radiative transfer calculations. Measured aerosol size distributions were used in these calculations and the optical properties were calculated using a MIE code assuming a complex refractive index of $1.4 + 0.01\ i$ that is representative of an European urban area [*Dubovik et al.*, 2002]. By comparing the computed reflectance with the one measured with OMI, the surface albedo and its wavelength dependence were derived using linear interpolation.

Figure 2 shows data for both a clean day (19 June 2005) with an aerosol optical depth of 0.097 ± 0.004 at 440 nm during the OMI overpass and a polluted day (23 June 2005) with an aerosol optical depth of 0.41 ± 0.01. Figure 2 shows the derived surface albedo for those two days in June 2004. The results for both days are very close. The surface albedo is indeed low in this wavelength domain, but we also observe a definite wavelength dependence with an increase of 30% between 400 and 470 nm.

[24] For the application of the multiwavelength algorithm at a global scale we developed a monthly mean surface albedo database using MISR data. In the MISR retrieval scheme the aerosol and surface properties are derived simultaneously. Furthermore, it is our experience that merging data sets with different spectral ranges, one in the visible and one in the UV for example, usually leads to discontinuities in the spectral surface albedo,which induce large errors in aerosol retrieval algorithms. The monthly mean
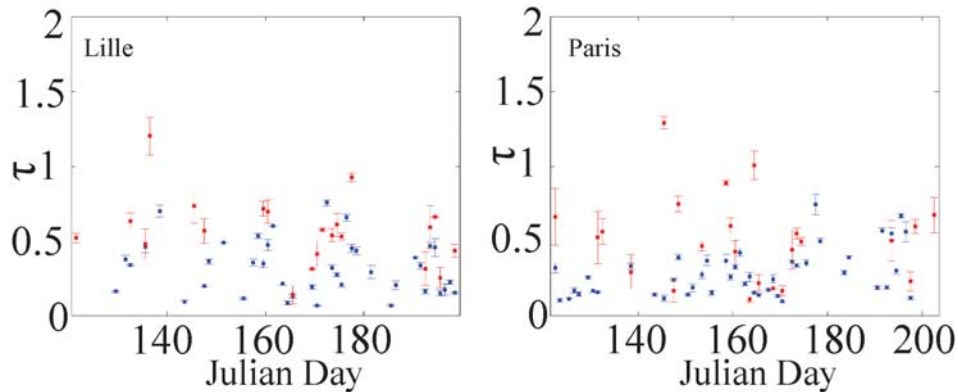

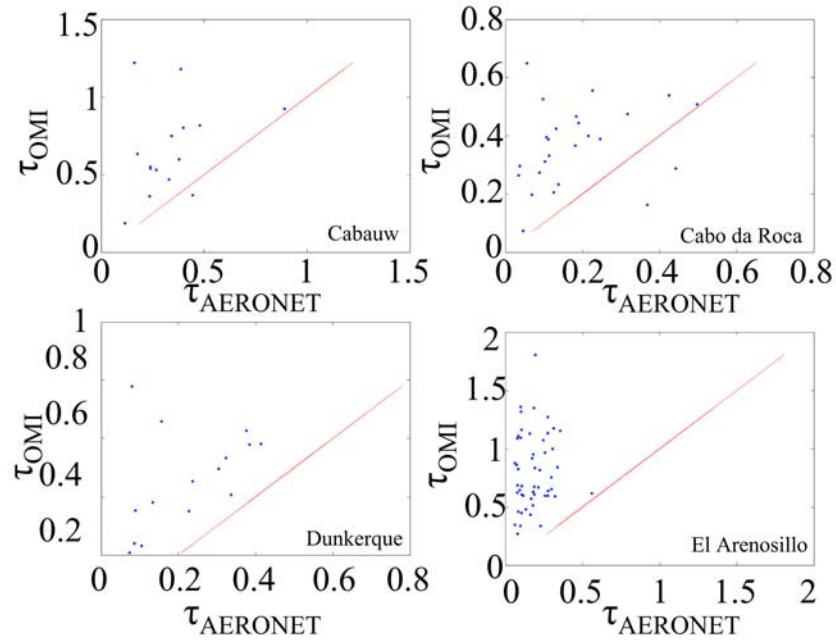**Figure 8.** Time series at 442 nm continued.

Figure 9. Scatterplot of the aerosol optical depth for May to July 2005 for several AERONET sites in western Europe. The red squares represent the spatially averaged aerosol optical depth retrieved at 442 nm from the multiwavelength algorithm within a 50 km radius of the ground site, and the error bars denote its standard deviation. The blue squares represent the averaged aerosol optical depth measured between 1100 UTC and 1400 UTC at 440 nm with a Sun photometer.

surface albedo database derived for the continents is based on MISR Component Global Land Surface Product Version F02 and F04, using five years worth of data Level 3 daily meshed product. The monthly minimum value of each meshed box was determined for the MISR bands at 446, 558 and 672 nm. From the surface albedo database derived

from GOME data [*Koelemeijer et al.*, 2003], it was concluded that a linear extrapolation of the 443 and 670 nm bands toward shorter wavelengths provide a reasonable estimation of the surface albedo in the UV range, over most surfaces. A minimum value of 1% for the surface albedo has been set for the extrapolation. For a small amount of
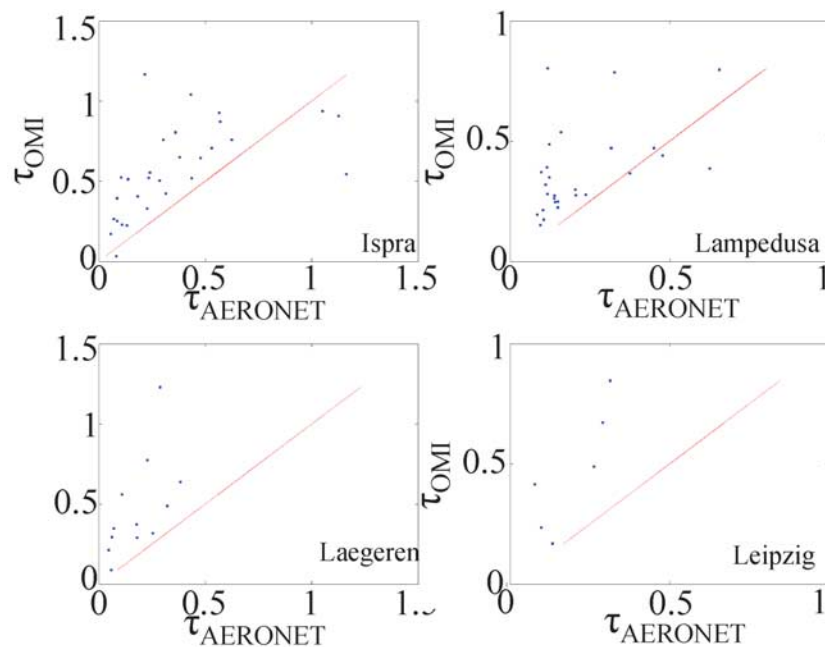

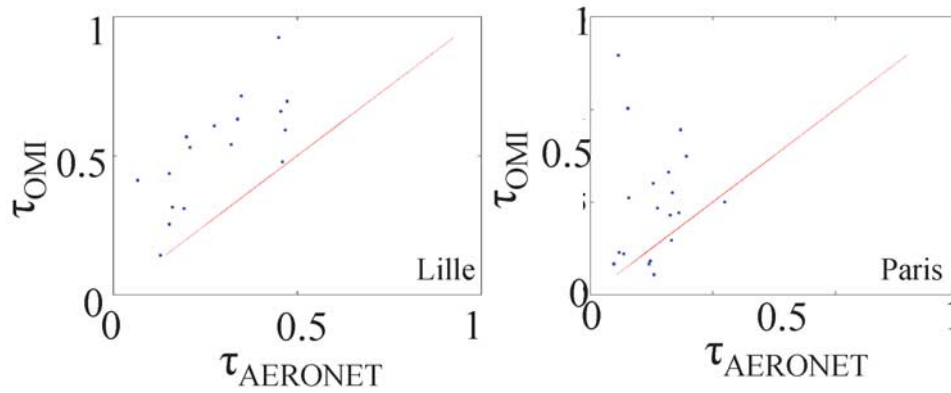**Figure 10.** Scatterplot continued.

Figure 11. Scatterplot continued.

meshed boxes no data were available and a cosmetic fill was applied. Theses boxes were filled using the nearest neighbor filling over a distance of at most one box. Finally, all remaining empty boxes were filled using the GOME surface albedo database.

[25] The spectral dependence of surface albedo derived for Cabauw, Figure 2, compares well with the surface albedo database derived from MISR. The surface albedo database derived from MISR compares favorably with TOMS and MODIS over vegetated surfaces whereas over dry surfaces, i.e., desert, the values tend to be lower for the MISR database.

3.3. Cloud Screening

[26] When clouds are present they dominate the TOA reflectance. Criteria applied to discriminate between cloud-free pixels and clouded pixels strongly depend on the cloud-screening purpose. The transition between aerosol and cloud is often gradual, so any cloud-screening protocol leads to a dilemma. Either too many pixels are rejected and a considerable amount of data is lost, or a known bias is accepted due to cloud contamination. In case of the multiwavelength algorithm three tests are performed, as described below, to determine whether a given pixel is cloud contaminated.

3.3.1. Reflectance Threshold Combined With Aerosol Absorption

[27] The first test is based on the UV aerosol index and the value of the reflectance at 388 nm. The presence of cloud result in near-zero values for the UV aerosol index [Hsu et al., 1996]. When the UV aerosol index is near or below zero and the measured reflectance at 388 nm exceeds a fixed threshold, the pixel will be flagged as cloud contaminated and rejected from further analysis. For this study the threshold for the reflectance was set at 0.3 and for the UV aerosol index at 0.12.

3.3.2. Cloud Fraction Test

[28] All pixels with effective cloud fraction larger than a preset threshold value are rejected. To determine this threshold, we take advantage of the A-train formation by synergistic use of Moderate Resolution Imaging Spectroradiometer (MODIS) on the Aqua satellite and the OMI instrument on Aura. OMI passes over the same area as MODIS within 15 minutes.

[29] MODIS provides a cloud mask grid [Ackerman et al., 2002]. Clouds are generally characterized by higher reflectance and lower temperature than the underlying earth surface. MODIS cloud detection takes place in the visible and infra-red range. Each test fails or succeeds depending on whether the pixel passes a given threshold. Each threshold is determined by the ground surface, the relative humidity, the aerosol load and the viewing angle.

[30] OMI is only sensitive in the UV-visible range. An effective cloud fraction [Acarreta et al., 2004] is retrieved from OMI data by comparing the measured reflectances to reflectances which are computed for both a cloud-free pixel and a fully cloudy pixel assuming a surface Lambert equivalent albedo of 0.8. The cloud fraction thresholds defined for the aerosol algorithm were determined by combining the cloud mask derived from MODIS and the cloud fraction from OMI. In order to do so, MODIS data have been meshed within the OMI grid for each matching orbit and compared to the OMI cloud fraction. Ideally, a given scene would be flagged the same way by both OMI and MODIS and yet it is not, as the assumptions are not the same for both algorithms. So as to define the cloud fraction threshold, a high correlation between MODIS and OMI diagnostic, as well as a stricter flagging in the MODIS case,

Table 3. Direct Comparison of OMAERO Data and AERONET Measurements[a]

Station	R	P	ndata	Cutoff
Cabauw	0.0168	0.9608	15	10
Cabo da Roca	0.2897	0.2593	23	10
Dunkerque	0.4508	0.1413	16	10
El Arenosillo	0.6237	1.7×10^{-5}	52	10
Leipzig	0.4512	0.4457	7	10
Ispra	0.4191	0.0370	33	10
Laegeren	0.4952	0.2121	10	10
Lampedusa	0.1311	0.4746	40	10
Lille	0.6400	0.0463	14	10
Paris	0.6050	0.0219	18	10

[a]Shown are the correlation coefficient, R, and probability, P, of getting a correlation as large as the observed value by random chance, when the true correlation is zero. When P is small, the correlation, R, is significant. ndata is the amount of available data, and cutoff represents the percentage of discarded data at each end of the data set, to compute P and R.
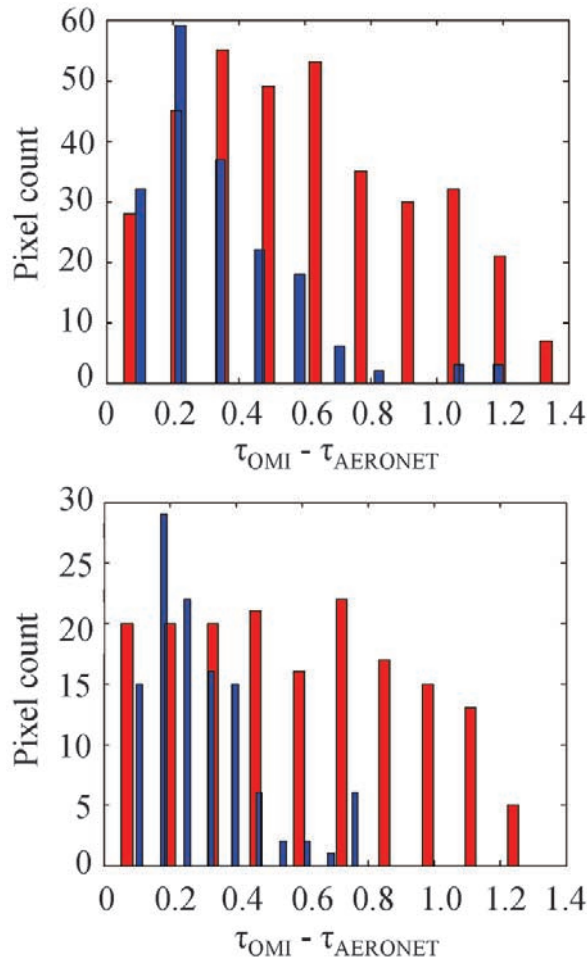
Figure 12. Histogram of the differences between the aerosol optical depth derived from OMI data and the aerosol optical depth measured for (top) El Arenosillo (37.1°N, 6.7°W) and for (bottom) Cabo da Roca (38.77°N, 9.5°W). Blue represents the pixels over the ocean, and the pixels over land are shown in red.

were expected. Following these requirements a cloud fraction threshold of 0.075 has been determined for this study.

3.3.3. Homogeneity Test: Small Pixel Variability Threshold

[31] Cloud free areas and thick clouds are more homogeneous than broken cloud fields. So the homogeneity within an OMI pixel can provide information on whether the pixel is cloud contaminated. The standard deviation within an OMI ground pixel is defined by means of the small pixel radiances. Small pixels are ground pixels with the same spatial resolution in the cross-track direction as the standard OMI ground pixel whereas in the in-flight direction they are smaller [*van den Oord et al.*, 2002]. These pixels correspond to one column pixels (i.e., wavelength) of the charge-coupled device (CCD) for which no co-addition was done. It allows determining the standard deviation threshold for which an OMI pixel is set as not clear. In this study the radiances' standard deviation threshold has been set at 1×10^{20} photons s^{-1} nm^{-1} cm^{-2} sr^{-1} (which corresponds to about 0.00015% of typical values of the small pixel variance).

3.3.4. Cloud Screening: Example

[32] Figure 3 (top) is an RGB picture from MODIS where clouds are visible for 14 June 2005. Figure 3 (bottom) shows the cloud mask derived from the OMI multiwavelength algorithm for the same day. The pixels marked as cloudy by all tests are colored in red. Cloudy pixels detected by the coherence spatial test are yellow, and the cloud free pixels are blue. The areas determined as cloudy by the cloud fraction test are colored purple.

[33] Figure 4 (top) is a composite map which presents a comparison of the cloud mask derived from MODIS [*Ackerman et al.*, 2002] and the cloud mask derived from OMI. In order to derive this composite map, the OMI cloud mask has been meshed into the MODIS cloud mask grid. The cloud-screening protocol from OMI has two positions, pixels are either cloudy or clear. In the MODIS cloud-screening protocol, pixels can be flagged in four different ways, cloudy, probably cloudy, probably clear or clear. Therefore, each pixel information from OMI and MODIS have been combined into an unsigned integer, such as the two first bits code for MODIS cloud mask and the third one for the OMI cloud mask. Table 2 summarizes and gives interpretations for each observed value in the combined cloud mask Figure 4 (top). The bottom of Figure 4 is a histogram of the available pixels for this comparison. It can be seen that 66.22% of the pixels have been flagged the same way by MODIS and OMI. Both cloud masks were in complete disagreement for 20.5% of the pixels. This occurs mainly over cloud edges, in this case 81% of the pixels were set as cloudy by OMI whereas MODIS set them as clear, therefore, this disagreement can mainly be explained by the size of an OMI pixel. For 13.28% of the pixels the comparison is not conclusive as the pixels were flagged as probably clear or uncertain by MODIS.

4. Results and Validation for Western Europe

[34] In this section the derived aerosol optical depth from OMI measurements by means of the multiwavelength algorithm is validated. The validation is done in three steps, in section 4.1 the aerosol optical depth retrieved from OMI is compared to ground measurement data. section 4.2 presents a comparison between OMI retrieval and another spaceborne instrument, MODIS. Finally, monthly averaged composite maps of the aerosol optical depth are analyzed in section 4.3.

4.1. Comparison Between OMI and Ground Measurements

[35] In order to check the accuracy of the OMI multiwavelength algorithm, the aerosol optical depth retrieved was compared with collocated Sun photometer data that are available from AERONET (http://aeronet.gsfc.nasa.gov/). The OMI derived aerosol optical depth at 442 nm was compared to the AERONET aerosol optical depth at 440 nm. The sites used for the validation were selected throughout Europe for their representativeness for different types of surfaces and aerosols; see Figure 5. OMI derived aerosol optical depths were averaged over an area of 50 km radius to provide a mean value for the ground site. The AERONET data (level 2, version 2) were used as available on the AERONET home page and the averaged of the aerosol
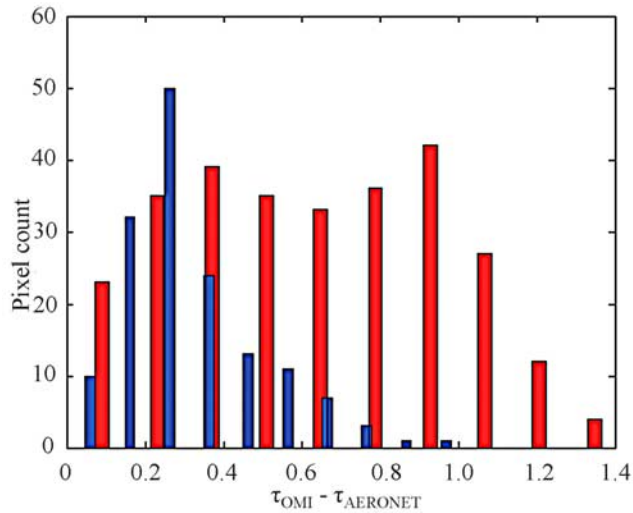
Figure 13. Same as top panel of Figure 12 assuming that the new location of the El Arenosillo ground site is 37.1°N, 7.2°W.

optical depth measured between 1100 UTC and 1400 UTC at 440 nm was computed for comparison.

[36] Figures 6 to 11 show the comparison between the OMI- and AERONET-retrieved aerosol optical depths, for the sites considered. Table 3 presents the correlation coefficient, R between OMI and AERONET data set. In general the agreement is within the standard deviation of the OMI area average, for both small and large aerosol optical depth values and for all sites considered except for El Arenosillo and Cabo da Roca. We also see some outliers which are discussed below. For every single ground site the OMI results trace the AERONET data. It appears that averaging the aerosol optical depth values over 50 km around a site may not be representative for highly polluted areas such as Ispra and Paris where there are significant gradients in the spatial distribution of the aerosol optical depth. However, spatial averaging is necessary to reduce pixel to pixel variability and provide a statistical significant result. In the comparisons for Cabauw and Dunkerque there are some outliers (marked by arrows), where the retrieved values are much higher than the AERONET aerosol optical depth. Likely, cloud screening in these cases was not strict enough.

[37] Besides cloud contamination, one of the main sources of discrepancy between satellite retrieved and measured aerosol optical depth is the effect of the surface albedo. The El Arenosillo and Cabo da Roca sites are perfect examples of the consequences of a wrong estimation of the surface albedo. Similar patterns in the retrieved and measured aerosol optical depth values, but with a positive bias, indicates that one of our a priori assumptions could be wrong. Likely this is due to an underestimation of the surface contribution to the TOA reflectance over land. Figure 12 presents a histogram of the difference between the AERONET aerosol optical depth and the OMI aerosol optical depth respectively for El Arenosillo and Cabo da Roca. The pixels above water are colored in blue and the pixels over land are colored in red. As expected the differ-

ences are larger over land than over sea. This is very clearly observed in the data for Cabo da Roca. For El Arenosillo the differences are less obvious. This is explained mainly by the geolocation of the measurement sites and the size of the OMI pixels. It is possible that some pixels flagged as sea include both land and sea resulting in erroneous correction for the surface contribution. Figure 13 presents the same data as for Figure 12a but for the processing it was assumed that the measurement site was displaced 0.5° toward the sea, which results in better discrimination between sea and land pixels with a move of the sea pixels histogram to small values of the difference.

[38] The comparison between the AERONET Sun photometer data and the OMI derived data for a variety of sites indicates that the aerosol optical depth trends are well reproduced by the multiwavelength algorithm but with a positive bias, albeit this derived surface albedo is not reliable in coastal areas such as El Arenosillo and Cabo da Roca. Ongoing work to derive surface albedos from OMI itself is expected to be finalized in fall of 2007.

4.2. Comparison Between OMI and MODIS

[39] MODIS and OMI are on different satellites in the A-train. The MODIS instrument is dedicated to, among others, monitoring aerosol and it is often used as a reference for comparison with other data. Because MODIS and OMI view the same area within 15 minutes, the aerosol optical depth distribution should be very similar. Therefore we evaluate the results derived from OMI at 471 nm versus the MODIS aerosol optical depth at 470 nm. MODIS aerosol data (collection 4) have been meshed into the OMI grid for Europe. The observed area is located between latitudes 60°N and 35°N and longitudes 25°E and 15°W. For this study 178081 cloud free pixels were available. The comparison has been done for 161528 pixels of the total available. Indeed, only the pixels entirely composed by MODIS pixels of a same surface type were selected. Table 4 gives an overview of available pixels.

[40] The results for land and sea pixels are presented separately because both the multiwavelength algorithm and the MODIS algorithm apply different methods to account for the surface reflection. Over water surfaces an ocean color model accounting for a wind surface speed-dependent surface roughness [Cox and Munk, 1954] is used. Over bright surfaces the multiwavelength algorithm uses a surface albedo database and the MODIS land algorithm derives the surface contribution to the TOA reflectance from measurement at 2130 nm [Remer et al., 2005]. Figures 14 to 16 present scatter density plots of the aerosol optical depth derived from OMI versus the aerosol optical depth derived from MODIS for May to July 2005. There is a clear correlation between both data sets, but also a systematic bias that indicates a tendency for OMI to overestimate the

Table 4. Amount of Pixels Used for the OMI Versus MODIS Comparison

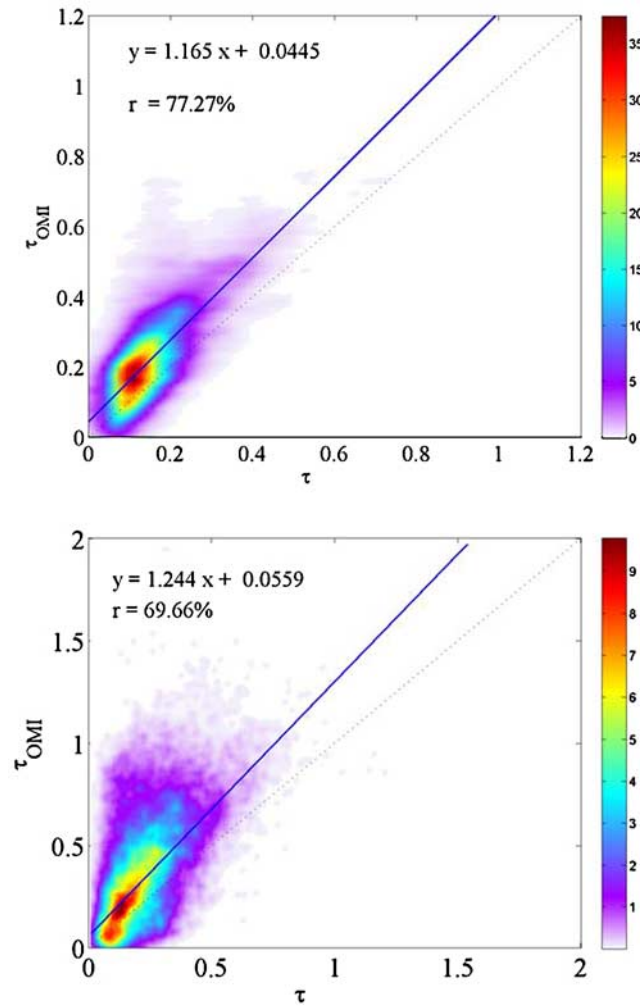| Month	Total	Sea Pixels	Land Pixels
May	47356	16265	26875
June	64724	17724	40845
July	66001	21034	38785

Figure 14. Scatter density plot of the aerosol optical depth at 471 nm derived from OMI data as a function of the aerosol optical depth at 470 nm derived from MODIS data over western Europe for May 2005. The top panel represents sea pixels, and the bottom panel shows land pixels.

places. Aerosol optical depth values as high as 1 are observed in some areas over Germany, Belgium, The Netherlands and Northern Italy whereas aerosol optical depth values of 0.2 to 0.4 were observed over Denmark and Ireland.

[42] Northern Italy presents a situation with a strong spatial gradient due to the presence of the Alps which provides a natural barrier for transport of aerosol produced in the heavily industrialized areas in the Po Valley (Milano, Torino). Hence these aerosols can only be ventilated through the Po Valley to the Adriatic Sea.

[43] The Iberian peninsula which contains the only European desert, presents an unrealistic pattern. Indeed, a severe drop of the aerosol optical depth is observed across the coast, which denotes clearly that the surface reflectance contribution over land is underestimated. This behavior is also observed for the time series of El Arenosillo and Cabo da Roca.

[44] In June, the average aerosol optical depth values are lower across Europe, but the heavily industrialized areas are still noticeable. To better understand these values the aerosol optical depth composite map has been compared to the NO_2 composite map, Figure 18, derived from the NRT OMI algorithm [*Boersma et al.*, 2006]. Aerosols and
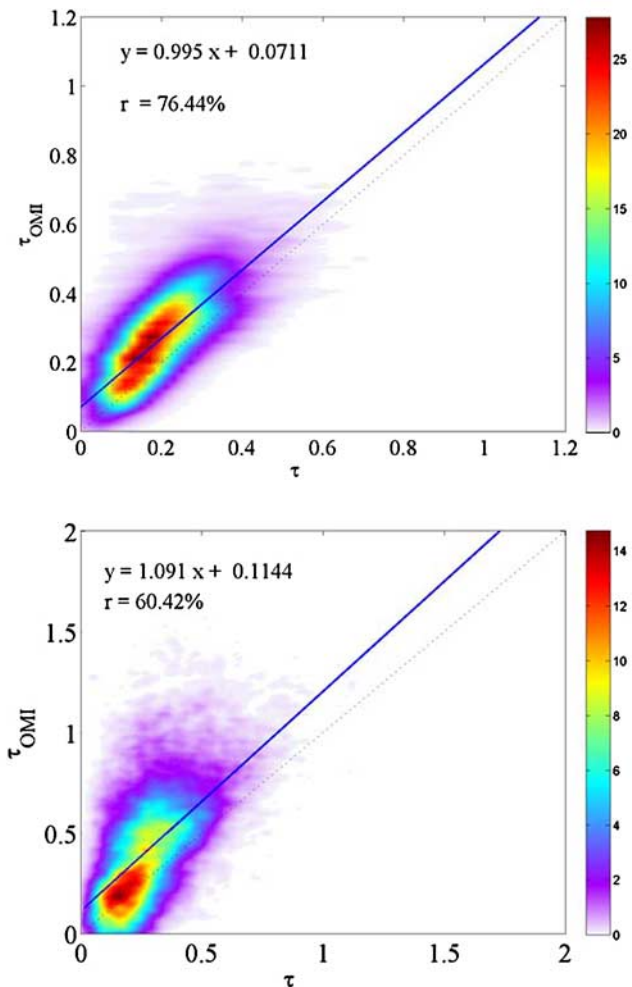
aerosol optical depth value with respect to MODIS. The correlation coefficient indicates that the multiwavelength algorithm performs better over sea than over land. This illustrates the limitation of the surface database used in this study. The lower correlation over land is also explained by the fact that MODIS over land is less reliable than over sea [*Remer et al.*, 2002; *Chu et al.*, 2002]. It is noted that after completion of this study, collection 5 data has become available with global aerosol optical depth values significantly lower than for collection 4.

4.3. Spatial Variation of the Aerosol Optical Depth

[41] Figure 17 shows a composite map of the monthly aerosol optical depth at 442 nm over Europe for May to July 2005. The white areas indicate the occurrence of either cloud or high surface albedo. They present a large variation in the aerosol optical depth over Europe. The high aerosol optical depth values are associated with highly industrialized areas whereas low values are observed at remote

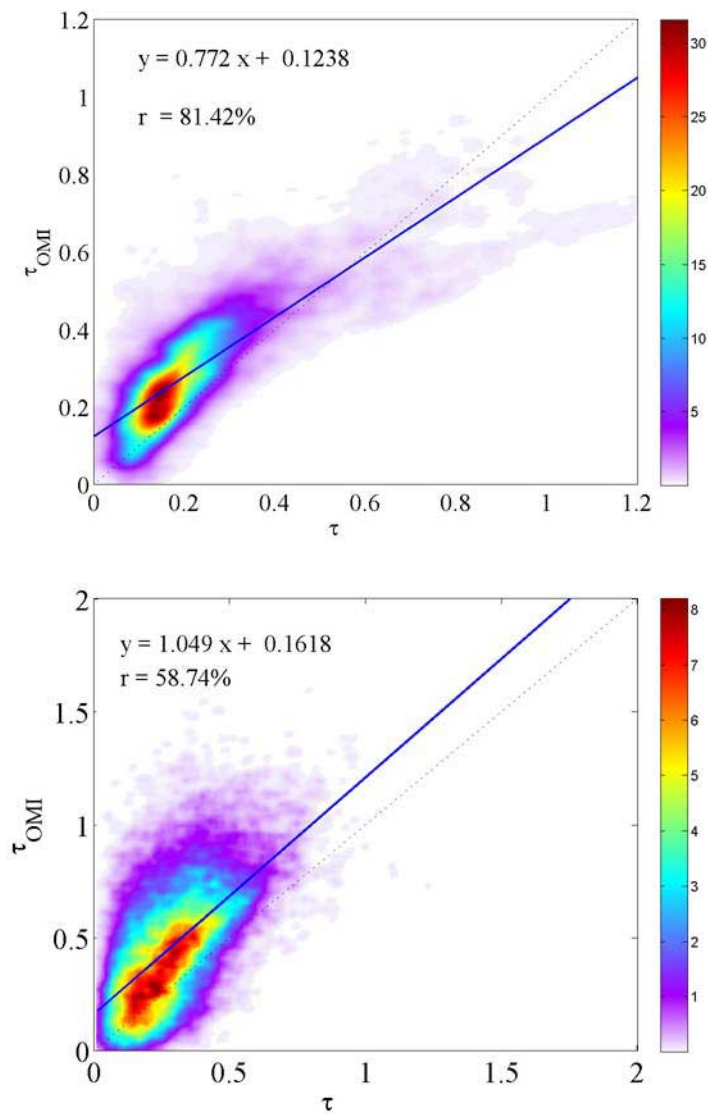**Figure 15.** Same as Figure 14 for June 2005.

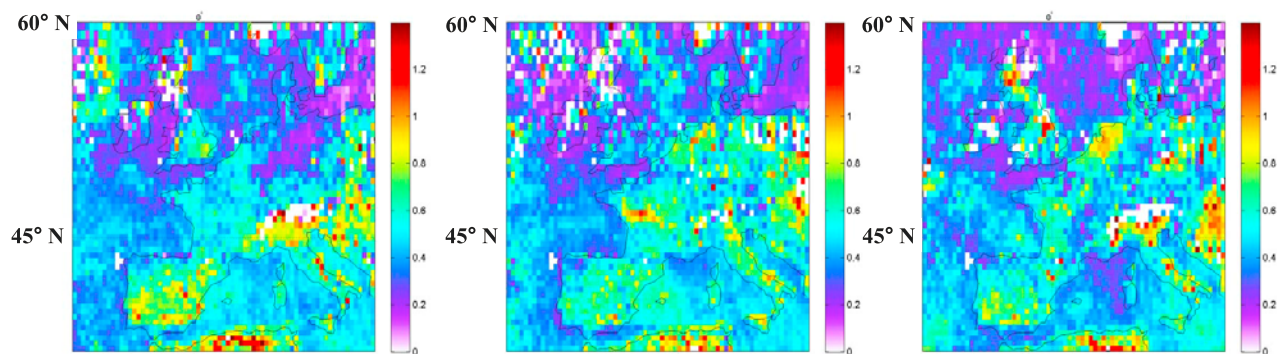Figure 16.   Same as Figure 14 for July 2005.

Figure 17.   Composite map of the aerosol optical depth at 442 nm over Europe for (left) May, (middle) June, and (right) July 2005. Aerosol optical depth has been retrieved by applying the multiwavelength method to OMI satellite data. White areas indicate that no mean values were computed.
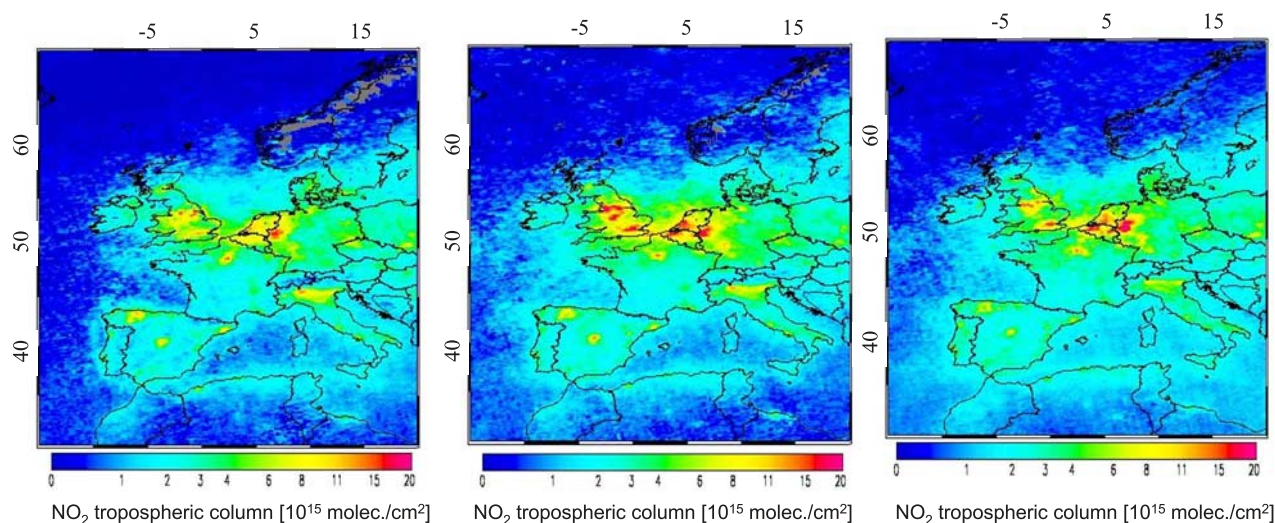
Figure 18. Composite map of spatial variation of the nitrogen dioxide tropospheric column (10^{15} molec.cm^{-2}) over Europe for (left) May, (middle) June, and (right) July 2005. Gray areas indicate that no mean values were computed.

NO_2 are both produced by anthropogenic activities so the observation of the NO_2 tropospheric column composite map can help to better understand the aerosol composite map. Owing to the short lifetime of NO_2, monitoring the NO_2 concentration allows for the identification of source regions. The variation of the monthly mean concentration in NO_2 does not imply a reduction of the activities. The NO_2 concentration appears to be lower in May than in June, whereas the monthly mean observed for July and June are similar. Comparison of the NO_2 concentration and the aerosol optical depth maps indicates that the low aerosol optical depth values observed in June are in part due to a difference in the meteorological conditions resulting in a difference in the transport. The aerosol optical depth composite map for July presents very high values from Orleans (47.9°N, 1.9°E) to Nantes (47.23°N, 1.58°W). Unfortunately no ground-based data were available for this area.

[45] Table 5 summarizes the monthly mean aerosol optical depth measured or derived for Cabauw, Ispra and Paris. The AERONET mean values were computed using all available aerosol optical depth measured between 1100 UTC and 1400 UTC. The OMI mean aerosol optical depth used all available values derived within a radius of 50 km to the ground site. As observed earlier the aerosol optical depth values derived from OMI are higher than their measured counterparts. However, the monthly mean values reproduce qualitatively the aerosol optical depth evolution across Western Europe.

5.   Conclusion and Perspectives

[46] The aerosol optical depth retrieved by means of the OMI multiwavelength algorithm has been compared to ground-based and satellite data. A major source of uncertainty in the retrieval of aerosol optical properties over land is the surface albedo. The ground-based data from the DANDELIONS campaign allowed us to derive the spectral dependance of the surface albedo which is representative for almost all Europe for this time period. Unfortunately this a

priori constraint still remains a problem for the Iberian peninsula. This may be solved when a more reliable surface albedo database will be available. A surface albedo database is currently being developed on the basis of OMI observations.

[47] Another major problem in aerosol remote sensing is the inability to retrieve aerosol properties in the presence of clouds. Therefore, accurate cloud detection is crucial. The cloud-screening procedure, developed for the OMI multiwavelength algorithm, is found to be satisfactory as MODIS and OMI cloud mask agree in 76.36% of the conclusive cases. In the cloud-screening protocol the OMI pixel's size remains the main drawback for area such as cloud edges or broken cloud fields. Both the sensitivity of the multiwavelength algorithm for retrieval of aerosols over various terrains and better cloud screening remain to be explored.

[48] Presented results from the OMI multiwavelength algorithm show that the time series for different sites over Europe compare favorably with the AERONET values. The direct ground-based observations and the OMI derived aerosol optical depth show similar trends in spite of the size of the OMI pixels. The correlation between OMI and AERONET data is as high as 0.6 for ground sites such as Lille, Paris and El Arenosillo, about 0.4 for Ispra and no significant correlation was found for the other ground sites. The aerosol optical depth derived from the multiwavelength algorithm also correlates well with the MODIS aerosol optical depth. A correlation coefficient of 0.66 over land and 0.79 over sea was derived for the period from May to July 2005. The correlation is better over dark water surfaces than over bright land surfaces, although the latter is still quite reasonable. However, there is a bias in the OMI versus MODIS comparison with an apparent overestimation of the OMI aerosol optical depth. The situation over land is expected to improve when the OMI-based surface albedo database becomes available and can be used in the aerosol optical depth retrieval over land.

[49] The spatial distribution of the aerosol optical depth over Europe for May, June and July 2005 was derived from OMI data. The retrievals show strong horizontal aerosol

Table 5. Monthly Mean Aerosol Optical Depth Derived From AERONET and OMI Data[a]

	OMI			AERONET		
Location	May	June	July	May	June	July
Cabauw	0.89	0.53	0.75	0.41	0.36	0.45
Ispra	0.78	0.84	0.50	0.38	0.42	0.29
Paris	0.56	0.53	0.55	0.40	0.32	0.40

[a]The monthly mean aerosol optical depth computed from all available aerosol optical depth measured between 1100 UTC and 1400 UTC. The OMI monthly mean aerosol optical depth computed from all available aerosol optical depth derived within a radius of 50 km to the ground site.

optical depth gradients with high aerosol optical depth values in the vicinity of highly industrialized area and low values around remote places.

References

Acarreta, J. R., J. F. De Haan, and P. Stammes (2004), Cloud pressure retrieval using the O_2-O_2 absorption band at 477 nm, *J. Geophys. Res.*, *109*, D05204, doi:10.1029/2003JD003915.

Ackerman, A. S., K. Strabala, W. Menzel, R. Frey, C. Moeller, L. Gumley, F. Schaaf, R. B. A. Baum, and G. A. Riggs (2002), Discriminating clear-sky from cloud with MODIS, ATBD-MOD-06, NASA, Washington, D. C. (Available at http://modis.gsfc.nasa.gov/data/atbd/)

Boersma, F. K., et al. (2006), Near-real time retrieval of tropospheric NO_2 from OMI, *Atmos. Chem. Phys. Discuss.*, *6*, 12,301–12,345.

Brinksma, E. J., M. Roozendael van, T. Wagner, O. Ibrahim, A. Richter, F. Wittrock, H. Oetjen, G. Pinardi, C. Hermans, and C. Fayt (2005), DANDELIONS Campaign held at the Cabauw Experimental Site for Atmospheric Research, The Netherlands, meeting report, Atmos. Composition Change Eur. Network of Excellence, Rome. (Available at http://troposat.iup.uni-heidelberg.de/AT2/Reports_and_papers/2005_12_Dandelions.htm)

Chu, D. A., Y. J. Kaufman, C. Ichoku, L. A. Remer, D. Tanré, and B. N. Holben (2002), Validation of MODIS aerosol optical depth retrieval over land, *Geophys. Res. Lett.*, *29*(12), 8007, doi:10.1029/2001GL013205.

Cox, C., and W. Munk (1954), Statistics of the sea surface derived from sun glitter, *J. Mar. Res.*, *13*, 198–227.

de Graaf, M., P. Stammes, O. Torres, and R. B. A. Koelemeijer (2005), Absorbing Aerosol Index: Sensitivity analysis, application to GOME and comparison with TOMS, *J. Geophys. Res.*, *110*, D01201, doi:10.1029/2004JD005178.

de Haan, J. F., P. B. Bosma, and J. W. Hovenier (1987), The adding method for multiple scattering calculations of polarized light, *Astron. Astrophys.*, *183*, 371–391.

Dentener, F., et al. (2006), Emissions of primary aerosol and precursor gases in the years 2000 and 1750, prescribed data-sets for AeroCom, *Atmos. Chem. Phys.*, *6*, 4321–4344.

Dubovik, O., N. Holben, T. F. Eck, A. Smirnov, Y. J. Kaufman, M. D. King, D. Tanre, and I. Slutsker (2002), Variability of absorption and optical properties of key aerosol types observed in worldwide locations, *J. Atmos. Sci.*, *59*, 590–608.

Haywood, J., and O. Boucher (2000), Estimate of the direct and indirect radiative forcing due to tropospheric aerosol: A review, *Rev. Geophys.*, *38*(4), 513–543.

Herman, B. M., and E. Celarier (1997), Earth surface climatology at 340 nm and 380 nm from TOMS data, *J. Geophys. Res.*, *102*, 12,059–12,076.

Holben, B., et al. (1998), Aeronet—A federated instrument network and data archive for aerosol characterization, *Remote Sens. Environ.*, *66*, 1–16.

Hsu, N. C., J. R. Herman, P. K. Bhartia, C. J. Seftor, O. Torres, A. M. Thompson, J. F. Gleason, T. F. Eck, and B. N. Holben (1996), Detection of biomass burning smoke from TOMS measurements, *Geophys. Res. Lett.*, *23*, 745–748.

Kinne, S., et al. (2006), An AeroCom initial assessment optical properties in aerosol component modules of global models, *Atmos. Chem. Phys.*, *6*, 1815–1834.

Koelemeijer, R. B. A., J. F. de Haan, and P. Stammes (2003), A database of spectral surface reflectivity in the range 335–772 nm derived from 5.5 years of GOME observations, *J. Geophys. Res.*, *108*(D2), 4070, doi:10.1029/2002JD002429.

Levelt, P. F., E. Hilsenrath, G. W. Leppelmeier, G. H. J. van Oord, P. K. Barthia, J. Tamminen, J. F. de Haan, and J. P. Veefkind (2006a), Science objective of the Ozone Monitoring Instrument, *IEEE Trans. Geosci. Remote Sens.*, *44*(5), 1199–1208.

Levelt, P. F., G. H. J. van Oord, M. R. Dobber, M. Malkki, H. Visser, J. de Vries, P. Stammes, J. Lundell, and H. Saari (2006b), The Ozone Monitoring Instrument, *IEEE Trans. Geosci. Remote Sens.*, *44*(5), 1093–1101.

Levy, R. C., L. A. Remer, S. Mattoo, E. F. Vermote, and Y. J. Kaufman (2007), Second-generation operational algorithm: Retrieval of aerosol properties over land from inversion of Moderate Resolution Imaging Spectroradiometer spectral reflectance, *J. Geophys. Res.*, *112*, D13211, doi:10.1029/2006JD007811.

Mie, G. (1908), Beitrge zur Optik trber Medien, speziell kolloidaler Metallsungen, *Ann. Phys. Leipsig*, *25*, 377–445.

Remer, L. A., et al. (2002), Validation of MODIS aerosol retrieval over ocean, *Geophys. Res. Lett.*, *29*(12), 8008, doi:10.1029/2001GL013204.

Remer, L. A., et al. (2005), The MODIS aerosol algorithm, products, and validation, *J. Atmos. Sci.*, *62*, 947–973.

Schoeberl, M. R., et al. (2006), Overview of the EOS Aura mission, *IEEE Trans. Geosci. Remote Sensing*, *44*, 1066–1074.

Stammes, P. (2000), Spectral radiance modelling in the UV-visible range, in *Proceedings of the International Radiation Symposium 2000: Current Problems in Atmospheric Radiation*, edited by W. L. Smith and Y. M. Timofeyev, A. Deepak, Hampton, Va.

Torres, O., P. K. Bhartia, J. R. Herman, Z. Ahmad, and J. Gleason (1998), Derivation of aerosol properties from satellite measurements of backscattered ultraviolet radiation: Theoretical basis, *J. Geophys. Res.*, *103*(D14), 17,099–17,110.

Torres, O., P. K. Bhartia, J. R. Herman, A. Sinyuk, P. Ginoux, and B. Holben (2002a), A long-term record of aerosol optical depth from TOMS observations and comparison to AERONET measurements, *J. Atmos. Sci.*, *59*(3), 398–413.

Torres, O., R. Decae, J. P. Veefkind, and G. de Leeuw (2002b), OMI Aerosol Retrieval Algorithm, in *OMI Algorithm Theoritical Basis Document*, vol. III, *Clouds, Aerosols and Surface UV Irradiance, ATBD-OMI-03*, edited by P. Stammes and R. Noordhoek, pp. 46–71, KNMI, De Bilt, Netherlands. (Available at http://www.knmi.nl/omi/research/documents)

van den Oord, B. H. J., P. Veefkind, P. Levelt, T. Jhonson, K. Stefanidis, A. Fleig, and R. Noordhoek (2002), OMI small pixel data, TN-OMIE-KNMI-397, KNMI, De Bilt, Netherlands. (Available at http://www.knmi.nl/omi/research/documents)

Veefkind, J. P., G. de Leeuw, and P. A. Durkee (1998), Retrieval of aerosol optical depth over land using two angle view satellite radiometry during TARFOX, *Geophys. Res. Lett.*, *25*(16), 3135–3138.

Veefkind, J. P., G. de Leeuw, P. Stammes, and B. A. Koelemeijer (2000), Regional distributions of aerosols over lands derived from ATSR-2 and GOME, *Remote Sens. Environ.*, *74*, 377–386.

Veihelmann, B., P. F. Levelt, P. Stammes, and J. P. Veefkind (2007), Simulation study of the aerosol information content in OMI spectral reflectance measurements, *Atmos. Chem. Phys. Discuss.*, *7*, 1785–1821.

Vermote, E. F., and A. Vermeulen (1999), Atmospheric correction algorithm: Special reflectances (MOD09), ATBD version 4.0, NASA, Washington, D. C. (Available at http://modis.gsfc.nasa.gov/data/atbd/)

von Hoyningen-Huene, W., M. Freitag, and J. B. Burrows (2003), Retrieval of aerosol optical thickness over land surfaces from top-of-atmosphere radiance, *J. Geophys. Res.*, *108*(D9), 4260, doi:10.1029/2001JD002018.

Wanner, W., A. H. Strahler, B. Hu, P. Lewis, J.-P. Muller, X. Li, C. L. B. Schaaf, and M. J. Barnsley (1997), Global retrieval of bidirectional reflectance and albedo over land from EOS MODIS and MISR data: Theory and algorithm, *J. Geophys. Res.*, *102*(D14), 17,143–17,161.

————————————

R. Braak, J. P. Veefkind, and B. Veihelmann, KNMI, P.O. Box 201, NL-3730 AE De Bilt, Netherlands.

R. L. Curier, Atmospheric Modeling and Observations, Climate Change Unit, Finnish Meteorological Institute, Erik Palménin Aukio 1, P.O. Box 503, FI-00101 Helsinki, Finland. (lyana.curier@gmail.com)

G. de Leeuw, Research and Development, Finnish Meteorological Institute, Erik Palménin Aukio 1, P.O. Box 503, FI-00101 Helsinki, Finland.

O. Torres, NASA Goddard Space Flight Center, Code 613.3, Greenbelt, MD 20771, USA.